Inamdar, Akbar I., Salunke, Amol S., Hou, Bo , Shrestha, Nabeen K., Im, Hyunsik and Kim, Hyungsang 2023. Highly durable and sustainable copper-iron-tin-sulphide (Cu2FeSnS4) anode for Li-ion battery: Effect of operating temperatures. Dalton Transactions 52 (34) , pp. 12020-12029. 10.1039/D3DT01338C

Publishers page: http://dx.doi.org/10.1039/D3DT01338C

Highly durable and sustainable copper-iron-tin-sulphide (Cu_2FeSnS_4) anode for Li-ion battery: Effect of operating temperatures

Akbar I. Inamdar,[1, *] Amol S. Salunke[1], Bo Hou,[2, §], Nabeen K. Shrestha,[1] Hyunsik Im[1, *] Hyungsang Kim[1, *]

[1]Division of Physics and Semiconductor Science, Dongguk University, Seoul 04620, Republic of Korea

[2] Department of Engineering Science, University of Oxford, Parks Road, OX1 3PJ, UK

[§] Present address: School of Physics and Astronomy, Cardiff University, Cardiff, CF24 3AA, Wales, UK.

Operating temperatures considerably influence the energy storage mechanism of the anode of Li-ion batteries (LiBs). This effect must be comprehensively studied to facilitate the effective integration of LiBs in practical applications and battery management. In this study, we fabricated a novel anode material, i.e., copper iron tin sulphide (Cu_2FeSnS_4, CFTS) and investigated the corresponding LiB performance at operating temperatures from 10 C to 55 C. The CFTS anode exhibited a discharge capacity of 283.1 mAhg ^{1} at room temperature (25 C), which stabilized to 174.0 mAhg ^{1} in repeated cycles tested at a current density of 0.1 Ag^{-} .^{1}The discharge capacity at higher operating temperatures such as 40 C and 55 C, is found to be 209.3 and 230.0 mAhg respectively. In contrast, the discharge capacity decreased to 36.2 mAhg ^{1} when the temperature decreased to 10 C. Electrothermal impedance spectroscopy was performed to determine the rate of chemical reactions, mobility of active species, and change in internal resistance at different operating temperatures. In terms of the cycle life, the CFTS exhibited outstanding cycling stability for more than 500 charge/discharge cycles, with a 146 % capacity retention and more than 80% Coulombic efficiency. The electrochemical investigation revealed that the charge storage in the CFTS anode is attributable to capacitive-type and diffusion-controlled mechanisms.

***Corresponding Authors**

*E-mail: akbarphysics2002@gmail.com, hyunsik7@dongguk.edu, hskim@dongguk.edu

Introduction

With the rising costs of gasoline and growing concerns regarding greenhouse gas emissions, hybrid electric (HEVs) and electric vehicles (EVs) have attracted significant attention. Owing to the need for portable storage devices in such vehicles, rechargeable Li-ion batteries (LiBs) have emerged as the ideal alternatives. LIBs are promising energy storage devices to store the energy generated from renewable energy sources. It can be applied for powering hybrid/full EVs, portable electronic gadgets, power tools, and various electric grids. Owing to their promising properties like high-energy, high-power density, environmental friendliness, and durability, LiBs can help develop an energy-sustainable economy.[1] Given these advantages, LiBs have attracted significant attention from research institutes, industries, and government agencies and are expected to dominate next-generation energy storage technologies. Nevertheless, several technical challenges associated with Li-ion batteries must be addressed before HEVs and EVs can achieve widespread market saturation. First, the energy and power densities depend on the operating temperatures. Second, promising alternatives to graphite as an anode material of LiBs must be identified, because even though graphite is inexpensive and chemically stable, its theoretical capacity (372 mAhg ^{1}) is exceptionally low, and its kinetics are slow.[2, 3]

LiBs must be carefully monitored and controlled (both electrically and thermally) to prevent potential fire hazards and deteriorated performance levels.[4, 5] The optimal operating temperatures for LiBs are 20 ï40 °C, and they exhibit adequate performance between -10 °C and 50 °C.[6] In particular, LiBs rapidly degrade in hot temperature environments, whereas their power output and energy decrease in cold temperature environments, leading to diminished performance and shortened range.[7] Many researchers have used analytical and numerical modelling techniques to estimate and predict the temperature of LiBs.[8] The potential of tin-based compounds as anode materials for LiBs has been explored, given their low cost, lack of toxicity, and high theoretical capacity of 994 mAhg^{-1}.[9] Compared with that of binary tin-based materials, the electronic conductivity of electrodes can be improved by the induction of Cu in the reaction with Li^+ during the discharge/charge process.[10] Considering this aspect, chalcogen materials have received considerable attention as a dopant to prepare alloy-type materials to boost the conductivity and stability of LiBs. Given their many benefits, such as a high theoretical capacity (FeS_2 890 mAhg^{-1}, CuS 560 mAhg^{-1}), safety, environmental friendliness and low cost,[11, 12] metal sulphides, especially FeS_2 and CuS, have been extensively researched. Heteroatom doping is the most widely used strategy to increase the conductivity of materials. Recently, quaternary compounds have attracted significant interest as potential anode materials.[13-19] Due to their exceptional theoretical reversible charge storage capacity, alloy-type materials and metal chalcogenides are remarkable LiB materials. Notably, although many studies have focused on the charge and discharge performance of LiB composites at ambient temperature, research on the performance of LiB composite anodes at high or low temperatures is limited.[20-24] Among quaternary chalcogenide materials, the application of copper zinc tin sulphide (Cu_2ZnSnS_4; CZTS) in LiBs has been widely explored, due to ability of structural flexibility for volume expansion.[25-28] However, the impact of the operating temperature on LiBs using CFTS anodes remains to be clarified. To facilitate the material application, the effect of the operating temperature on the electrochemical LIB performance of CFTS must be studied.

Therefore, in this work, we fabricated a CFTS anode through a one-step hydrothermal technique and studied its electrochemical performance in the LiB at different operating temperatures. The average specific capacity of the CFTS anode was noted to be 174.0 mA h g^{-1} (at room temperature (25 C)) tested at a current density of 0.1 Ag^{-1}. In long cycle life testing at 25 C (500 cycles), the anode exhibited 146% and 80% of capacity retention and Coulombic efficiency respectively. The effect of different operating temperatures on the electrochemical performance, occurred due to change in the internal resistance of the CFTS anode, was explored.

Experimental section

Fabrication of CFTS

Cu_2FeSnS_4, a quaternary chalcogenide was synthesized via a one-step hydrothermal technique. The chemicals (copper chloride, iron chloride pentahydrate, ethylene glycol, and thiourea) were analytical grade and used as received. A 50 mL solution in ethylene glycol was prepared with molarities of 0.5, 0.25, 0.25 and 1.25 mM of copper chloride, iron chloride, tin chloride pentahydrate, and thiourea respectively. The magnetic stirrer was used to mix the solution for 10 min. The prepared solution was transferred to a Teflon-lined autoclave container that was then placed in the furnace at 220 C for one day (24 h). The CFTS powder was collected by centrifuging the final product at 7000 rpm for 10 min, and it was then dried in oven for overnight. Finally, the agate mortar was used to ground the collected powder for 3 h and used to fabricate LiB anodes.

Characterizations

The X-ray diffractometer (made in Netherlands with a model name of PANalyX ô pcPRO) ô s was used to analyse the structural properties of CFTS anode. Raman spectra were measured using

Raman spectrophotometer named Labram Aramis spectrometer (made by Horiba Jobin) at wavelength of 514 nm. The surfaced morphology and composition were analysed through FeSEM-JSM-6701F made in Japan and EDAX) measurements at an operating voltage of 15 kV. Moreover, other structural properties like TEM, HRTEM, SAED and HADIF elemental mapping were performed using a JEM 2010 microscope (JEOL Ltd., made in Japan) and an EDX detector (Oxford Instruments) at operating voltage of 300 kV. The Ulvac-phi, Verse probe II modelled photoelectron spectroscopy was used to determine oxidation states CFTS anode.

Battery construction using the CFTS anode and electrochemical testing.

The CFTS anode was coated onto Cu foil paper by preparing a slurry using the doctor blade technique. The slurry was prepared using 80% CFTS powder, 10% polyvinylidene fluoride (PVDF) in N-methyl-2-pyrrolidone (NMP) as a binder, and 10% carbon black. Next, the slurry was coated manually onto the Cu-foil paper using doctor blade technique and dried in an oven. A standard CR2032 type coin cell was assembled using CFTS as the anode in a globe box filled with argon as a pure inert gas. The diameter of the CFTS anode was 15 mm, and the counter electrode was a Li metal disc. The electrolyte prepared with 1:1 ratio of ethylene carbonate and dimethyl carbonate as 1 M $LiPF_6$ was used. The LIB battery performances were tested using an MPG-2 battery cycler made by Bio-Logic Science Instruments, France.

Results and discussion

The structural characteristics of the CFTS anode were studied through the XRD patterns obtained at a scan rate of 2° per minute between 10°-80°. **Figure 1(a)** shows the XRD pattern of the as-prepared CFTS powder along with JCPDS no. 44-1476. The multiple peaks at 2θ angles 28.74°, 29.39°, 32.96°, 48.08°, and 59.32° with reflections along the (112), (103), (200), (204), and (224), respectively, are attributable to the Cu_2FeSnS_4 phase. The diffraction peaks other than those of the CFTS are attributable to the secondary phases of SnS at 26.6° (102), 31.76° (111), and 52.72° (112) (JCPDS-39-0354) and CuS at 32.92° (006), 49.05° (110), and 57.91° (109) (JCPDS-79-2321).[29, 30]. To obtain more details, Raman spectroscopy measurements were obtained at 540 nm. **Figure 1(b)** shows the Raman spectra of the CFTS anode coated onto the Cu foil paper. The broad main vibration band at 274 cm ^{1} is attributable to Cu_2FeSnS_4, whereas the other peaks at 208, 298, 384, and 482 cm ^{1} are associated with SnS (Eg mode), Cu_2SnS_3, $Cu_2Sn_3S_7$, and $Cu_{2-}S_x$, respectively. The XRD and Raman analyses reveal the existence of secondary phases (SnS and CuS) along with the quaternary CFTS phase. The large number of elements in CFTS cause difficulties in achieving a single phase and the ideal stoichiometry, which remains a key challenge in further improving device performance.

Figure1 (c) and Figure S1 (supporting information**)** show the SEM images (at different magnifications) of the CFTS powder coated onto the Cu foil paper. Grains of different sizes and randomly shaped plates are distributed all over the sample. The heterogeneously sized grains of the CFTS and its porous nature likely facilitate ion intercalation during charging/discharging. **Figure 1(d)** shows the digitized EDAX spectra of the CFTS anode, disclosing the existence of Cu, Fe, Sn, and S in the prepared materials. The original EDAX spectra and SEM image are provided in **Figure S2** (supporting information). The EDAX elemental mapping shown in **Figure S3** suggests the uniform distribution of Cu, Fe, Sn, and S in the sample.

The CFTS was also characterized by the TEM, HRTEM, SAED, HAADF-STEM and EDX elemental mapping techniques. **Figures 2(a)** and **2(b)** show the TEM and HRTEM images of CFTS respectively. The TEM image shows a nano granular structure, whereas the HRTEM image shows clear lattice edges, suggesting the polycrystalline nature of CFTS. The spacings between the two lattice fringes are 0.27 nm (**Figure 2(c)**) and 0.32 nm (**Figure 2(d)**), associated with the (200) and (112) reflections of Cu_2FeSnS_4. These values agree with standard JCPDS data card no. 44-1476, revealing the successful synthesis of the quaternary CFTS. The clear and bright spots observed in the SAED pattern (**Figure 2(e)**) are associated with the diffraction peak of Cu_2FeSnS_4 towards the (002), (200), (-200), and (2-22) planes, revealing the highly crystalline nature of the sample. The HAADF-STEM line scan (**Figure S4**, supporting information) and EDX elemental mapping images (**Figure 2(f)**) of the CFTS indicate the uniform distribution of Cu, Fe, Sn, and S in the sample, with the target compositions.

Figures 3(a–d) depicts the deconvoluted core level XPS spectra of Cu2p, Fe2p, Sn3d, and S2p. The survey spectrum is shown in **Figure S5,** which indicates the presence of all desired elements. The Cu2p spectrum in **Figure 3(a)** displays two main peaks at 932.6 eV for Cu $2p_{3/2}$ and 952.4 eV for Cu $2p_{1/2}$, which are associated with the Cu (I) as major species. The peaks at 934.2 eV and 954.0 eV associated with the Cu (II) minor species.[33, 34]. Fe2p spectrum is deconvoluted in two doublets, as shown in **Figure 3(b).** The first doublet of $Fe2p_{3/2}$ and $Fe2p_{1/2}$, at 711.5 and 723.6 eV, suggests the presence of Fe^{2+}. The second at 715.6 and 727.3 eV, is attributable to the Fe^{3+} states in the CFTS anode.[35, 36] The core level Sn 3d (**Figure 3(c))** shows peaks at 486.05 eV ($3d_{5/2}$) and 495.3 eV ($3d_{3/2}$), connected with the Sn^{2+} and Sn^{4+} oxidation states, respectively.[15] The high-resolution S2p spectrum shows peaks at 161.64 eV ($2p_{3/2}$) and 162.9 eV ($2p_{1/2}$), which are attributable to the sulphide phase, and at 169.0 eV ($2p_{3/2}$) and 170.4 eV, which are associated with sulphonate and Cu-S-O, respectively.[37] Thus, the XPS study suggest that the surface composition of the CFTS anode includes Cu^{1+}, Fe^{2+}, Sn^{2+}, and S^{2-}.

The lithium storage performance of the CFTS anode was evaluated by CV based on a CR 2032 type coin cell. **Figure 4(a)** shows the CV curve recorded at 0.1 mVs^{-1} scan rate in 0.01–3.0

V (vs. Li/Li$^+$) at room temperature. The change in the CV shapes, especially in the cathodic sweep, is considerably different than that in the following cycles, owing to the polarization and solid electrolyte interface (SEI) formation after lithiation.[37, 38] The pair of cathodic peaks at 1.4 V and 0.90 V in the first cycle are attributable to the irreversible conversion of Li_2S and reduction reaction of the CFTS anode to metallic states, respectively.[39, 40] During the reverse scan, anodic peaks are observed at 0.6 V and 1.23 V, which are correlated to the dealloying processes (reversible reaction) between constituent elements of the CFTS anode. The anodic peak at 2.3 V is presumably due to the decomposition/oxidation of the amorphous Li_2S. In the following cycles, the cathodic peak at approximately 0.65 V is attributable to the reversible reduction reaction to form metal species of CFTS. The impact of the operating temperature on the CVs of the CFTS is illustrated in **Figure S6** (supporting information). The CV curves do not change as the operating temperature increases, suggesting the highly sustainable and reversible electrochemical behaviours of the CFTS anode.

Figure 4(b) shows the galvanostatic charge–discharge (GCD) curves of the CFTS for the first five cycles, recorded at 0.1 Ag^{-1} in room-temperature conditions**.** The inclined voltage plateaus of the discharging and charging behaviours are due to the insertion and de-insertion of the Li$^+$ ions into the CFTS anode, respectively. The discharge and charge plateaus located at 0.65V and 0. 6 V are agreed with the CV profiles. The CFTS delivers a first discharge capacity of 283.1 mAhg^{-1}, which stabilizes to 174.0 mAhg^{-1} in the sixth cycle. The rapid decrease of the capacity is occurred from the SEI layer formation and structural reconstruction of the CFTS electrode.[37, 38] The transformation of the voltage plateaus from 0.9 in the 1st cycle to 0.65 V in the 6th cycle are in agreement with the cathodic peaks in the CV curves. The smaller specific capacity of the CFTS anode compared to its theoretical capacity (499 mAhg^{-1}) is due to the presence of the secondary phase in the electrode material. These secondary phases have a larger band gap than that of the CFTS, which affects the electronic and transport properties, hindering the movement of ions and electrons and presenting a large kinetic barrier.

To clarify the mechanisms associated with the insertion/extraction of Li^{2+} ions, we performed ex situ XRD, Raman and SEM (**Figure S7**) measurements in the fully charged (to 3.0 V) and discharged (to 0.01 V) states. The XRD pattern of the CFTS anode (**Figure S7(a)**) in the discharged state is consistent with an amorphous nature, although the Cu metal peaks associated with the current collector suggest the alloying of the electrode during lithiation. During de-lithiation, the electrode exhibited a peak at

which is attributable to the reconstruction (dealloying) of the electrode to the CFTS phase. The Raman spectra (**Figure S7 (b)**) of the CFTS in the discharged state indicate reduced peak intensity, potentially because of the partial conversion of the CFTS into amorphous Li_2S_x. By contrast, the spectra in the charged state exhibited a peak associated with the CFTS after dealloying. Thus, the ex-situ analysis in the charged and discharged states suggests that the CFTS electrode undergoes an alloying-type mechanism. The absence of any cracks in the SEM image after charging–discharging ((**Figures. S7 (c–d)**) suggests high durability and protection form the volume expansion of the CFTS.

The LiB performance at different operating temperatures must be studied because materials exhibit different kinetics and mobility at different temperatures, which affects the battery performance. Therefore, we investigated the performance of the CFTS anode at operating temperatures, varying from C to 55 C. **Figure 4 (c)** shows the GCD curves of the CFTS anode measured at 0.1 Ag^{-1}. The shape of the GCD curve does not change with the temperature, which indicates that the CFTS anode undergoes similar electrochemical reactions and has an outstanding thermal strength. The specific charge–discharge capacity of the CFTS anode increases with the increase in the operating temperatures: The capacity is 230.0 mAhg^{-1} at 55 C and 209.3 mAhg^{-1} at 40 C. The increased specific capacity high temperature with reduced voltage gap between the plateaus of charge and discharge are correlated with the enhanced reaction kinetics and its mobility. Thus, CFTS anode exhibit satisfactory performances at high temperatures (40 C) without any decrease in the specific capacity. At low operating temperatures, i.e. 10 C (**Figure S8**, supporting information) the specific capacity rapidly decreased to 36.2 mAhg^{-1}, potentially because of the increased charge transfer resistance (**Figure S9**) and reduced ionic conductivity of the CFTS.[41]

Moreover, the rate performance of the CFTS anode (**Figure 4(d)**) was investigated at different currents densities between 0.1 Ag^{-1} and 1.0 Ag^{-1}. The anode exhibits stable discharge capacity in all five cycles at current densities up to 1.0 Ag^{-1} and outstanding rate performance and reversible behaviour at 0.1 Ag^{-1}. Notably the CFTS anode shows enhanced specific capacity at 40 C and different current rates. Under different current rates, the specific discharge capacity of the CFTS is lower at 55 C than that at 40 C. The specific capacity of the CFTS measured at 55 C is superior (note that it is not reversible after 30 charge–discharge cycles) only at the lower current rate of 0.1 Ag^{-1}, which could probably be due to the increased reaction rate, mobility of active species and change in internal resistance. However, it deteriorates at a higher current rate ranging between 0.2 and 1.0 Ag^{-1}. Thus, the deterioration of the specific capacity is because of several factors such as i) ageing of the electrode at high temperature, ii) Li-plating at the anode, which is irreversible, iii) unwanted side reactions and iv) increase in the SEI thickness. Therefore, the existence of any of these factors causes sluggish interfacial kinetics as well as insufficient charge and mass transport properties of the electrodes at high current rates. Thus, the result agrees with other previously reported LIB materials. [42, 43]

The electrochemical long-term cycling performance in terms of the capacity retention and coulombic efficiency of the CFTS was studied at different operating temperatures at a current rate of 0.1 A g^{-1}. **Figures 5(a)** and **5(b)** present the capacity retention and coulombic efficiency data, respectively, of the CFTS studied at different operating temperatures. The discharge capacity of all three samples decreased first and then increased after 25 cycles at each operating temperature. After 100 cycles, the CFTS could retain 99% of its discharge capacity at 25 °C, whereas at 40 C and 55 C, it was found to be to 93% and 94%, respectively. The increase in the discharge capacity of the CFTS at 25 C after 20 cycles is due to the pseudocapacitive nature of the electrode, which is typical of conversion-type electrode materials.[44] Furthermore, the coulombic efficiency of the CFTS at different operating temperatures is in the range of 80%–90% [**Figure 5(b)]**, which suggests the excellent applicability of the electrode in LiBs. The temperature-dependent lithium storage performance was examined by electrochemical impedance spectroscopy measurements, as depicted in **Figure 5(c)**. The semicircle diameter and sloping line represent the charge transfer resistance (R_{ct}) and diffusion of lithium ions, respectively. The charge transfer resistance at 55 C is smaller than that at 25 C and 40 C, which supports the abovementioned results.

In addition, the CFTS was tested for very long cycle life of more than 500 cycles at 25 C, as shown in **Figure 5 (d)**. The initially decreases of discharge capacity and then increases after 25 cycles up to 500 cycles. A reversible capacity of 218 mAhg^{-1} was obtained even after 500 charge–discharge cycles, with an enhanced capacity retention of 146%. A steady-state coulombic efficiency (**Figure S10)** of more than 80% during the long cycle-life testing suggests the excellent reliability, reversibility and sustainability of the CFTS electrode for commercial LIBs. To determine the reason and mechanism for the capacity increase during 25–500 cycles, we performed ex situ XRD, SEM and EIS measurements (shown in **Figure S11** supporting information) before and after stability of the 500 cycles. In the XRD [**Fig. S11(a)**] analysis, the shift of the (103) diffraction peak towards a higher angle after prolonged lithiation processes suggests an increase in inter-layer spacing. This enlarged inter-layer spacing reduces the insertion resistance, which is beneficial to the diffusion of Li^{+}. This behaviour is also validated through EIS analysis (**Fig. S11(b)**), in which the reduction of charge transfer resistance to 29.88 q (compared to the original 35.00 q) is observed after a prolon**Fig. S11(c-** lithia **d)**] after the lithiation process shows a clear and robust nano-granular morphology, which exposes a greater surface area to the electrolyte. Thus, the phenomenon observed is agreement with that of the other anode materials reported in the literature for LIBs.[45,46] Thus, all these phenomena occurred in the CFTS during the long cycle-life study, facilitating the increase in the specific capacity of the battery. The total capacity of the CFTS anode at 25 C was quantitatively estimated using the CV measurements at various scan rates which is in terms of the capacitive and diffusion-limited contributions. **Figure 6(a)** depicts a CV curve of the CFTS anode, measured at different scan rates between 0.1 to 0.5 mVs^{1}. A power law (Eq. (1)) was used to estimate the kinetics of the Li-ion intercalation using the cathodic and anodic peak currents at different scan rates.[15, 38, 47]

$$i = a \quad {}^{b} \qquad\qquad (1)$$

where is the scan rate, a and b are the fitting parameters, and. The storage mechanism such as diffusion-controlled and capacitive is observed from the slope of the log(i) ī ( )plot, b (**Figure 6(b)**). Slopes lower than 0.5 and higher than 1.0 correspond to diffusion-controlled and capacitive-type storage mechanism, respectively. Slopes between 0.5 and 1.0 represent a combined storage mechanism. According to **Figure 6(b)**, from the cathodic and anodic peak currents, b is estimated to be 0.74 and 0.76 respectively. This finding suggests that the reaction current observed in the CFTS anode is attributable to the combined mechanism of intercalation and capacitive-type.

The capacitive and diffusion-controlled contributions from the obtained total current were quantitatively estimated using Eq. (2):

$$i = k_1 \quad + \; k_2 \; ^{1/2} \qquad (2)$$

where i is the current at a fixed potential, k_1 and k_2 are the fitting parameters. k_1 Î and k_2 Î$^{1/2}$ are the capacitive contribution, and diffusion-controlled contributions. The fitting parameters k_1 (slope of the curve) and k_2 (y-axis intercept) are estimated from the plot of Î$^{1/2}$ vs. $i/$ Î$^{1/2}$ (**Figure S12**). **Figures 6(c)** and **6(d), shows the** contributions of the capacitive and diffusion-controlled storage mechanisms. The decrease of capacitive contribution with respect to the scan rate, indicating that the capacitive-type and diffusion-controlled mechanisms are the dominant contributors at low and high scan rates, respectively.

Conclusions

We demonstrate the fabrication of quaternary Cu_2FeSnS_4 by hydrothermal technique and its sustainable Li-ion battery performance as an anode is tested at different operating temperatures. The impact of operating temperature on the charge storage capacity and its sustainability is discussed in detail. It exhibited a stable room temperature discharge capacity of 174.0 mAhg^{1} at 0.1 Ag$^{\bar{}}$.^{1}When it is tested at 40 C and 55 C the discharge capacity is enhanced to 209.3 and 230.0 mAhg respectively, whereas the poor performance observed when it is cooled at 10 C due to increased charge transfer resistance. The sustainability study at different operating temperatures revealed that, the CFTS had better activity at 40 C with to 104 % capacity retention and coulombic efficiency above 80 %. Moreover, the long cycle life testing at room temperature over 500 charge -discharge cycles prove the applicability of the CFTS as an anode in commercial LIBs. Further study revealed that the charge storage in the CFTS is due to capacitive type and diffusion-controlled contributions.

Acknowledgements

The authors would like to thank the financial support from the National Research Foundation (NRF) of Korea (Grant nos. 2021R1A2B5B01001796, 2022R1F1A070724, 2021R1A4A5031805).

Conflicts of Interest

The authors declare no competing financial interests.

Author contributions

A.I.I., N.K.S., H.K., and H. I. designed the experiments and wrote the manuscript. A.S S. carried out the experiments and extracted data for the analysis. B.H. carried out electron microscopy. All of the authors have reviewed and approved the final version of the manuscript.

Notes and References

[1] N. Nitta, F. Wu, J. T. Lee, G. Yushin, ñLi-ion battery materials: present and future,ò *Mater. Today,* vol. 18(5), pp. 252-264, 2015.

[2] X. Liu, T. Najam, G. Yasin, M. Kumar, M. Wa -Pot Synthesis of High-Performance Tin Chalcogenides/C Anodes for Li-Ion Batteries,ò *ACS Omega*, vol. 6, pp. 17391ī17399, 2021.

[3] M. C. Han, L. L. Zhu, Y. M. Li, F. Wei, Y. S Zn$_2$Ti$_3$O$_8$/g-C$_3$N$_4$ composites as anode materials for Li-ion batteries,ò *Dalton Trans.* vol. 50, pp. 11137-11146, 2021.

[4] S. Panchal, J. Mcgrory, J. Kong, R. Fraser, M. Fowler, I. Dincer, M. AgelinZChaab, ñCycli degradation testing and analysis of a LiFePO$_4$ battery at actual conditions,ò *Int. J. Energy Res.* vol. 41, pp. 2565ï2575, 2017.

[5] Y. AbdulZQuadir, T. Laurila, J. Karppinen, ñHeat prismatic LiZion battery cell with LiMnNiCoO$_2$ cathode material,ò *Int. J. Energy Res.* vol. 38, pp. 1424Z1437, 2014.

[6] M. Malik, I. Dincer, M. Rosen, ñReview on u management for electric and hybrid electric v *Int. J. Energy Res.* vol. 40, pp. 1011Z1031, 2016.

[7] B. Wu, V. Yufit, M. Marinescu, G. J. Offer, R. F. MartinezZBotas, N. P. Brando thermalZelectrochemical modelling of uneven heat generation in lithiumZion battery pac *J. Power Sources*, vol. 243, pp. 544Z554, 2013.

[8] S. Panchal, I. Dincer, M. AgelinZCha, R. Fraser, M. Fowler, ñThermal modeling and validation of temperature distributions in a prismatic lithiumZion battery at different discharge rates and varying boundary conditions,ò *Appl. Therm. Eng.* vol. 96, pp. 190Z199, 2016.

[9] J. Cabana, L. Monconduit, D. Larcher, M. Ros -Based Li-Ion Batteries: The State of the Art and Challenges of Electrode Materials Reacting Through Conversion Reactions, *Adv. Mater*, vol. 22. pp. E170 ïE192, 2010.

[10] H. C. Tao, S. C. Zhu, X. L. Yang, L. L. Zhang, S. Bing, ñReduced graphene oxide decorated ternary Cu_2SnS_3 as anode materials for lithium-ion batteries, *J. Electroanal. Chem*,ò vol. 760, pp. 127-134, 2016.

[11] J. Zhou, F. Jiang, S. Li, Z. Xu, W. Sun, X. Ji, Y. Yang, ñCu_2FeS as an anode material with an enhanced electrochemical performance for lithium-ion batteries fabricated from natural ore chalcopyrite, *J. Solid-State Electrochem.*ò vol. 23, pp. 1991 ï2000, 2019.

[12] M. Walter, T. Zuend, M. V. Kovalenko, ñPyr $_2$). nanocrystals as inexpensive high-performance lithium-ion cathode and sodium-ion anode materials, *Nanoscale*,ò vol. 7, no. 20, pp. 9158 ï9163, 2015.

[13] T. Kai, S. Haddadpour, H. F. Andersen, L. Mayrhofer, T. T. Järvi, M. Moseler, K. C. Möller, S. Dehnen, ñQuaternary Diamond-Like Chalcogenidometalate Networks as Efficient Anode Material in Lithium-Ion Batteries, *Adv. Funct. Mater*,ò vol. 23, pp. 5693 ï5699, 2013.

[14] W. H. Kan, A. Huq, A. Manthiram, ñExploration of a Metastabl Diagram for the Quaternary Li ïNi ïMn ïCo ïO System, *Chem. Mater.,*ò vol. 28, pp. 1832 ï1837, 2016.

[15] A. I. Inamdar, B. Hou, H. S. Chavan, A. S. Salunke, J. Han, G. Shin, S. Park, S. Yeon, N. K. Shrestha, H. Im, H. Kim, ñCopper cobalt tin sulphide (Cu$_2$CoSnS$_4$) anodes synthesised using a chemical route for stable and efficient rechargeable lithium-ion batteries, *Dalton Trans.*,ò vol. 51, pp. 14535-14544, 2022.

[16] A. I. Inamdar, H. S. Chavan, A. T. A. Ahmed, Y. Jo, S. Cho, J. Kim, S. M. Pawar, H. Kim, H. Im, “Macroporous Cu(OH)$_2$ nanorod network fabricated directly on Cu foil as binder-free Lithium-ion battery anode with high capacity”, *J. Alloys Compd.*, vol. 829, article 154593, 2020.

[17] S. M. Pawar, B. S. Pawar, Bo Hou, A. T. A. Ahmed, H. S. Chavan, Y. Jo, S. Cho, J. Kim, J. Seo, S. N. Cha, A. I. Inamdar, H. Kim and H -density CuCo$_2$O$_4$ nanosheets as a high-performance Li-ion battery materia *J. Ind. Eng. Chem.*, vol. 69, article 13, 2019.

[18] L. Mi, H. Sun, Q. Ding, W. Chen, C. Liu, H. Hou, Z. Zheng, C. Shen, “3D hierarchic patterned tubular NiSe with nano-/microstructures for lithium-ion bat *Dalton Trans.* vol. 41, pp. 12595-12600, 2012.

[19] H. Imagaw, H. Itahar, “Stabilized lithium-ion battery anode performance by calcium-bridging of two dimensional siloxene layers”, *Dalton Trans.* vol. 46, pp. 3655-3660, 2017.

[20] Q. Tang, H. Su, Y. Cui, A. P. Baker, Y. Liu, J. Lu, X. Song, H. Zhang, J. Wu, H. Yu, D. Qu, “Ternary tin-based chalcogenide nanoplates as a promising anode material for lithium-ion batteries”, *J. Power Sources*, vol. 379, pp. 182-190, 2018.

[21] Z. Su, K. Sun, Z. Han, F. Liu, Y. Lai, J. Li, Y. Liu, “Fabrication of ternary Cu–Sn–S sulfides by a modified successive ionic layer adsorpti *J. Mater. Chem.* vol. 22, pp. 16346-16352, 2012.

[22] J. Jaguemont, L. Boulon, Y. Dubé, “A comprehensive review of lithium-ion batteries used in hybrid and electric vehicles at cold temperatures”, *Appl. Energy*, vol. 164, pp. 99–114, 2016.

[23] Z. Yang, Q. Huang, S. Li, J. Mao, "High-temperature effect on electrochemical performance of $Li_4Ti_5O_{12}$ based anode material for Li-ion batteries," *J. Alloys Compd.*, vol. 753, pp. 192-202, 2018.

[24] M. J. Piernas-Muñoz, S. E. Trask, A. R. Dunlop, E. Lee, I. Bloom, "Effect of temperature on silicon-based anodes for lithium-ion batteries," *J. Power Sources*, vol. 441, article 227080, 2019.

[25] Z. Syum, T. Billo, A. Sabbah, B. Venugopal, S. Y. Yu, F. Y. Fu, H. L. Wu, L. C. Chen, K. H. Chen, "Copper Zinc Tin Sulfide Anode Materials for Lithium-Ion Batteries at Low Temperature," *ACS Sustainable Chem. Eng.*, vol. 9, no.27, pp. 8970-8979, 2021.

[26] J. Lin, J. Guo, C. Liu, H. Guo, "Three-Dimensional Cu_2ZnSnS_4 Films with Modified Surface for Thin Film Lithium-Ion Batteries," *ACS Appl. Mater. Interfaces*, vol. 7, article 17311, 2015.

[27] Q. Jiang, X. Chen, H. Gao, C. Feng, Z. Guo, "$_2ZnSnS_4$ as Novel Anode material for Lithium-ion Batteries," *Electrochimica Acta*, vol. 190, pp. 703-712, 2016.

[28] X. Yin, C. Tang, M. Chen, S. Adams, H. Wang, H. Gong, "Hierarchical porous Cu2ZnSnS4 films for high-capacity reversible lithium storage app," *J. Mater. Chem. A.*, vol. 1, pp. 7927-7932, 2013.

[29] Q. Xie, H. Zhou, Z. Lv, H. Liu, H. Guo, "Sn^{4+} self-doped hollow cubic SnS as an efficient visible-light photocatalyst for Cr(VI) reduction a," *J. Mater. Chem. A.*, vol. 5, pp. 6299-6309, 2017.

[30] B. M. Palve, V. S. Kadam, C. V. Jagtap, S. R. Jadkar, H. M. Pathan, "A simple chemical route to synthesis the CuSe and CuS counter electrodes for titanium oxide-based quantum dot solar cells," *J. Mater. Sci: Mater. Electron.,* vol. 28. Pp. 14394–14401, 2017.

[31] R. R. Prabhakar, N. H. Loc, M. H. Kumar, P. P. Boix, S. Juan, R. A. John, S. K. Batabyal, L. H. Wong, "Facile Water-based Spray Pyrolysis of Earth-Abundant Cu_2FeSnS_4 Thin Films as an

Efficient Counter Electrode in Dye-Sensitized Solar Cells,” *ACS Appl. Mater. Interfaces*, vol. 6. Pp. 17661-17667, 2014.

[32] P. A. Fernandes, P. M. P.Salomé, A. F. da Cunha, “Study of polycrystalline Cu_2ZnSnS_4 films by Raman scattering,” *J. Alloys Compd.*, vol. 509, pp. 7600–7606, 2011.

[33] C. Zhu, A. Osherov, M. J. Panzer, “Surface chemistry of electrodeposited Cu_2O films studied by XPS,” *Electrochimica Acta*, vol. 111, pp. 771–778, 2013.

[34] M. S. Alhumaimess, A. A. Essawy, M. M. Kamel, I. H. Alsohaimi, H. M. A. Hassan, “Biogenic-Mediated Synthesis of Mesoporous Cu_2O/CuO Nano-Architectures of Superior Catalytic Reductive towards Nitroaromatics,” *Nanomaterials,* vol. 10, no. 4, article 781, 2020.

[35] Y. Li, H. Zhang, M. Jiang, Q. Zhang, P. He -Supported Fe-Doped Ni_2P Nanosheet Arrays as Bifunctional Catalysts for Overall Water Splitting,” *Adv. Funct. Mater.*, vol. 27, article 1702513, 2017.

[36] L. M. Cao, Y. W. Hu, S. F. Tang, A. Iljin, J. W. Wang, Z. M. Zhang, T. B. Lu, Fe-CoP “Electrocatalyst Derived from a Bimetallic P Large-Current-Density Oxygen Evolution and Overall Water Splitting,” *Adv. Sci.*, vol. 5, article 1800949, 2018.

[37] A. I. Inamdar, R. S. Kalubarme, J. Kim, Y. Jo, H. Woo, S. Cho, S. M. Pawar, C. J. Park, Y. W. Lee, J. I. Sohn, S. Cha, J. Kwak, H. Kim, H. Im, “Nickel titanate lithium-ion battery anodes with high reversible capacity and high-rate long-cycle life performance,” *J. Mater. Chem. A.*, vol. 4, pp. 4691-4699, 2016.

[38] A. I. Inamdar, Abu Talha A. A, H. S. Chavan, Y. Jo, S. Cho, J. Kim, S. Pawar, B. Hou, S. N. Cha, H. Kim, H. Im, “Influence of operating t $Li_2ZnTi_3O_8$ anode performance and high-rate charging activity of Li-ion battery,” *Ceram. Int.*, vol. 44. pp. 18625-18632, 2018.

[39] T. Liu, G. Melinte, O. Dolotko, M. Knapp, B. Mendoza-Sánchez, “Activation electrodes induced by high-rate lithiation processes,” J. Energy Chem., vol. 78, pp. 56–70, 2023.

[40] G Bree, H. Geaney, K. Stokes, K. M. Ryan, “Copper Zinc Tin Sulfide Nanorods as Lithium-Ion Battery Anodes with High Specific Capacities,” *J. Phys. Chem. C*, vol. 122. pp. 20090–20098, 2018.

[41] M. Alipour, C. Ziebert, F. V. Conte, R. Kizilel, “A Review on Temperatu-Dependent Electrochemical Properties, Aging, and Performance of Lithium-Ion Cells,” *Batteries*, vol. 6, no. 3, article 35, 2020.

[42] C. Heubner, K. Nikolowski, S. Reuber, M. Schneider, M. Wolter, A. Michaelis, “Recent Insights into Rate Performance Limitations of Li-ion Batteries,” *Batteries & Supercaps*, vol. 4, pp. 268–285, 2021.

[43] G. Handel, K. Fauler, M. Kapper, C. Schmuck, R. Stangl, F. Fischer, S. Uhlig, J. Koller, “Thermal aging of electrolytes used in lithiu-ion batteries – An investigation of the impact of protic impurities and different housing materials,” *J. Power Sources,* vol. 267, pp. 255-259, 2014.

[44] Z. Li, H. Liu, J. Huang, Ŭ Zhang, “MOF-derived MoSe/C composites as anode materials for Li-ion batteries,” *Ceram. Int.*, vol. 45, pp. 23765–23771, 2019.

[45] J. Guo, Y. Li, J. Meng, K. Pedersen, L. G mechanism of capacity increase during early cycling of commercial NMC/graphite lithium-ion batteries,” *J. Energy Chem., vol.* 74, pp. 34–44, 2022.

[46] Y. Zhu, H. Li, Y. Wu, L. Yang, Y. Sun, G. Chen, Y. Liu, Z. Wu, C. Zhang, X. Guo, “Unveiling the abnormal capacity rising mechanism of MoS_2 anode during long-term cycling for sodium-ion batteries,” *RSC Adv.*, vol. 11. pp. 28488, 2021.

[47] S. Loua, X. Cheng, Y. Zhao, A. Lushington, J. Gao, Q. Li, P. Zuo, B. Wang, Y. Gao, Y. Ma, C. Du, G. Yin, X. Sun, “Superior performance $_2$O$_7$ anodes for lithium-ion batteries: Understanding from the structural and pseudocapacitive insights on achieving high-rate capability,” *Nano Energy*, vol. 34, pp. 15-25, 2017.

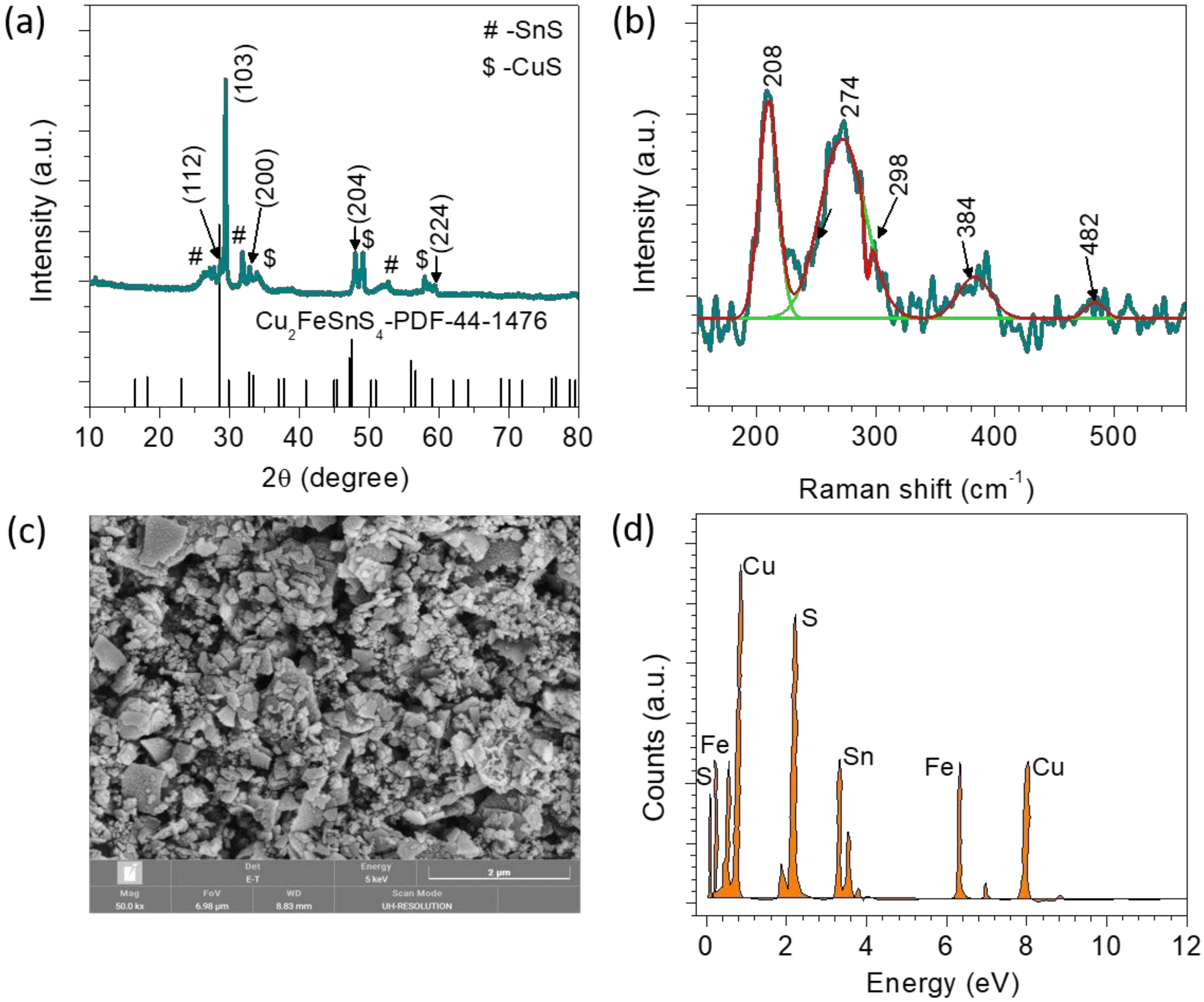

Figure 1. Structural investigations of the Cu_2FeSnS_4 (CFTS) anode fabricated by hydrothermal technique. (a) XRD patterns of the Cu_2FeSnS_4 structure in comparison with standard powder diffraction data of JCPDS 44-1476. (b) Raman spectrum, (c) scanning electron microscopy image, and (d) EDX spectrum of CFTS.

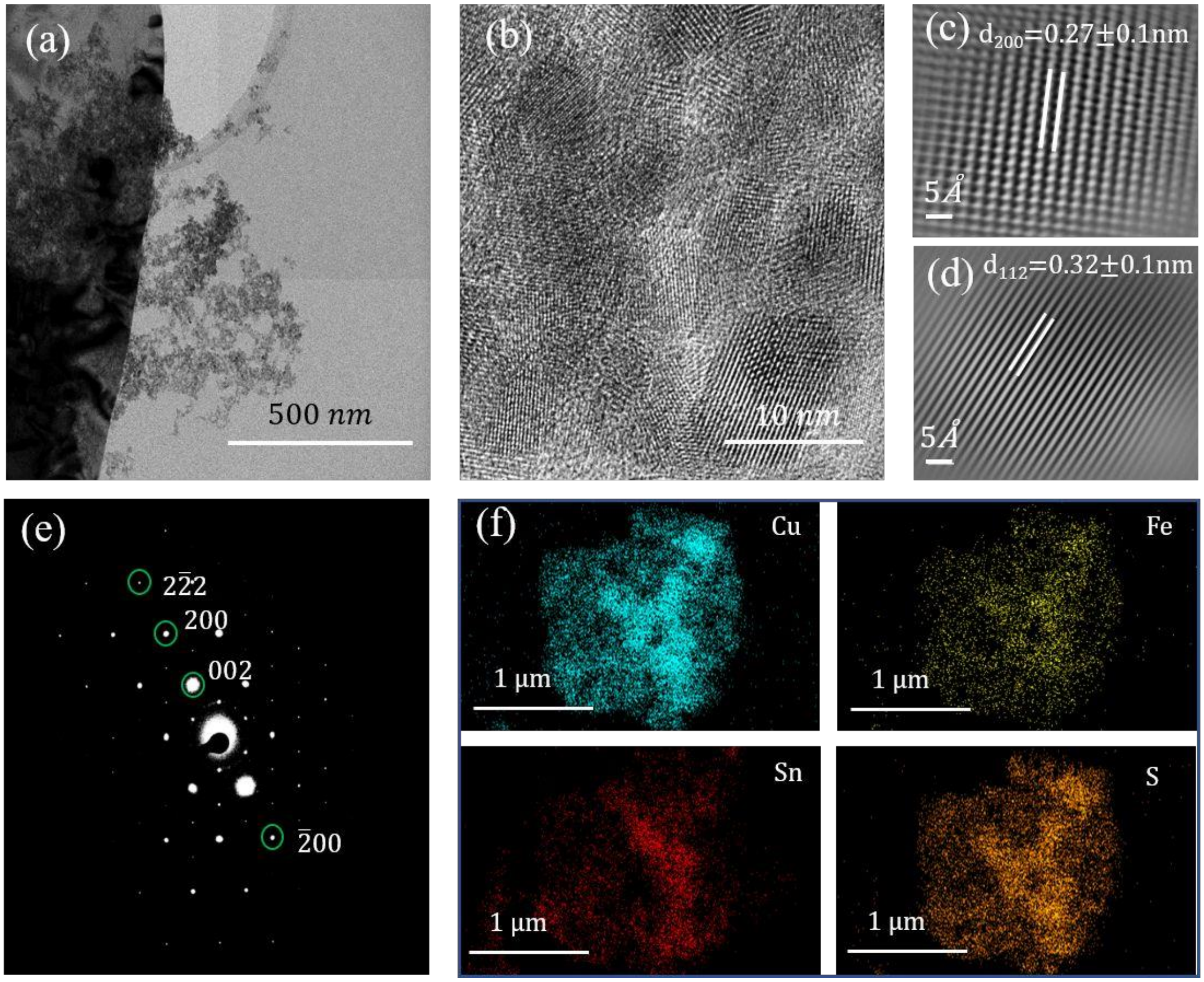

Figure 2. (a) TEM images of the CFTS anode. (b) High-resolution TEM (HRTEM) images. (c, d) Clear lattice fringes can be seen in the HRTEM image, revealing the crystalline nature of the CFTS anode. (e) SAED pattern. The clear bright spots are attributable to the highly crystalline nature of CFTS (JCPDS 44-1476). (f) HAADF-STEM elemental mapping under TEM mode, depicting the uniform distribution of Cu (dark cyan), Fe (yellow), Sn (red), and S (orange) in the sample.

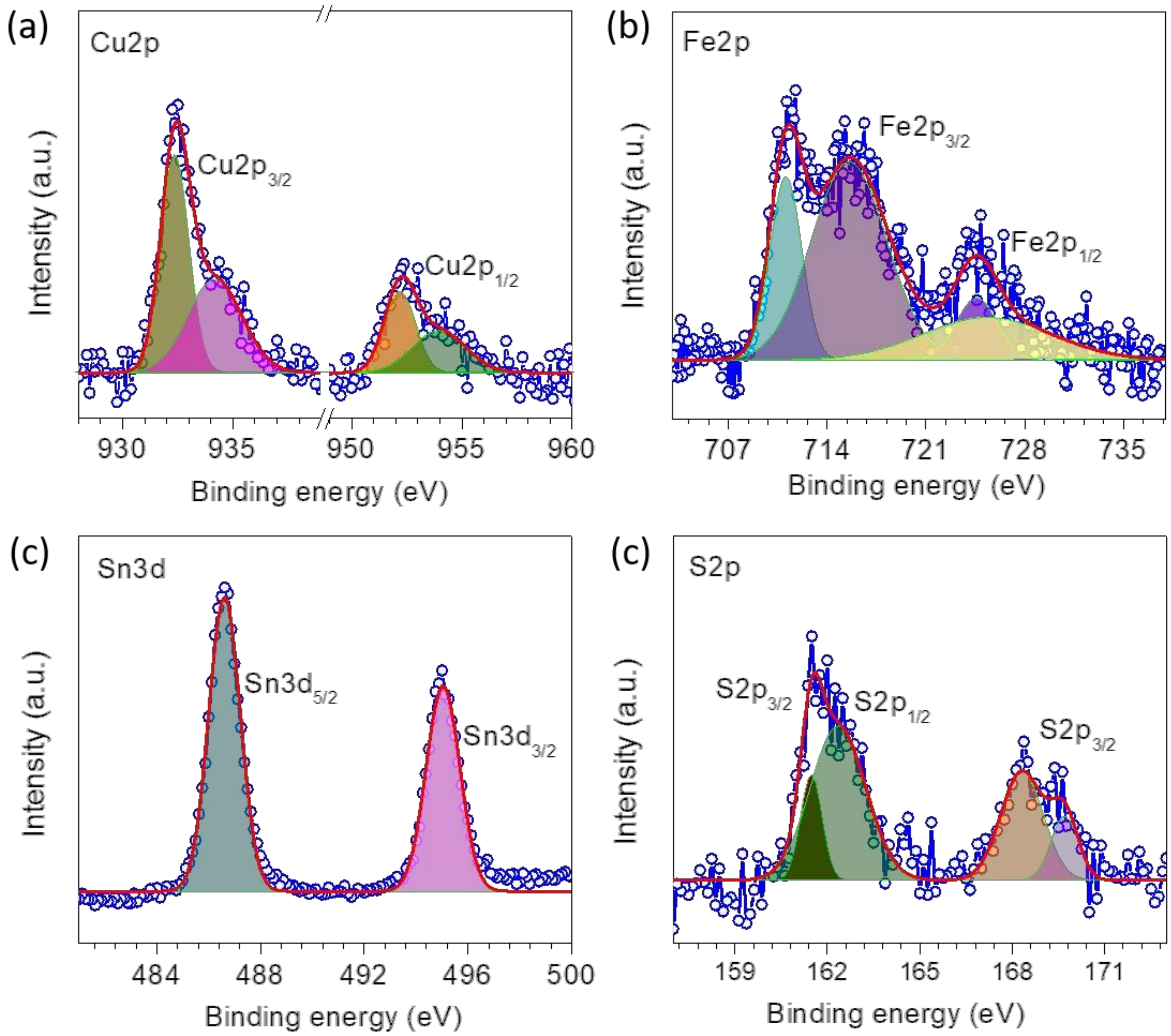

Figure 3. XPS spectra of the as-grown CFTS anode electrode. Deconvoluted XPS spectra of (a) Cu 2p, (b) Fe 2p, (c) Sn 3d, and (d) S 2p peaks. The experimental data and fitted curves are denoted with circles and lines respectively.

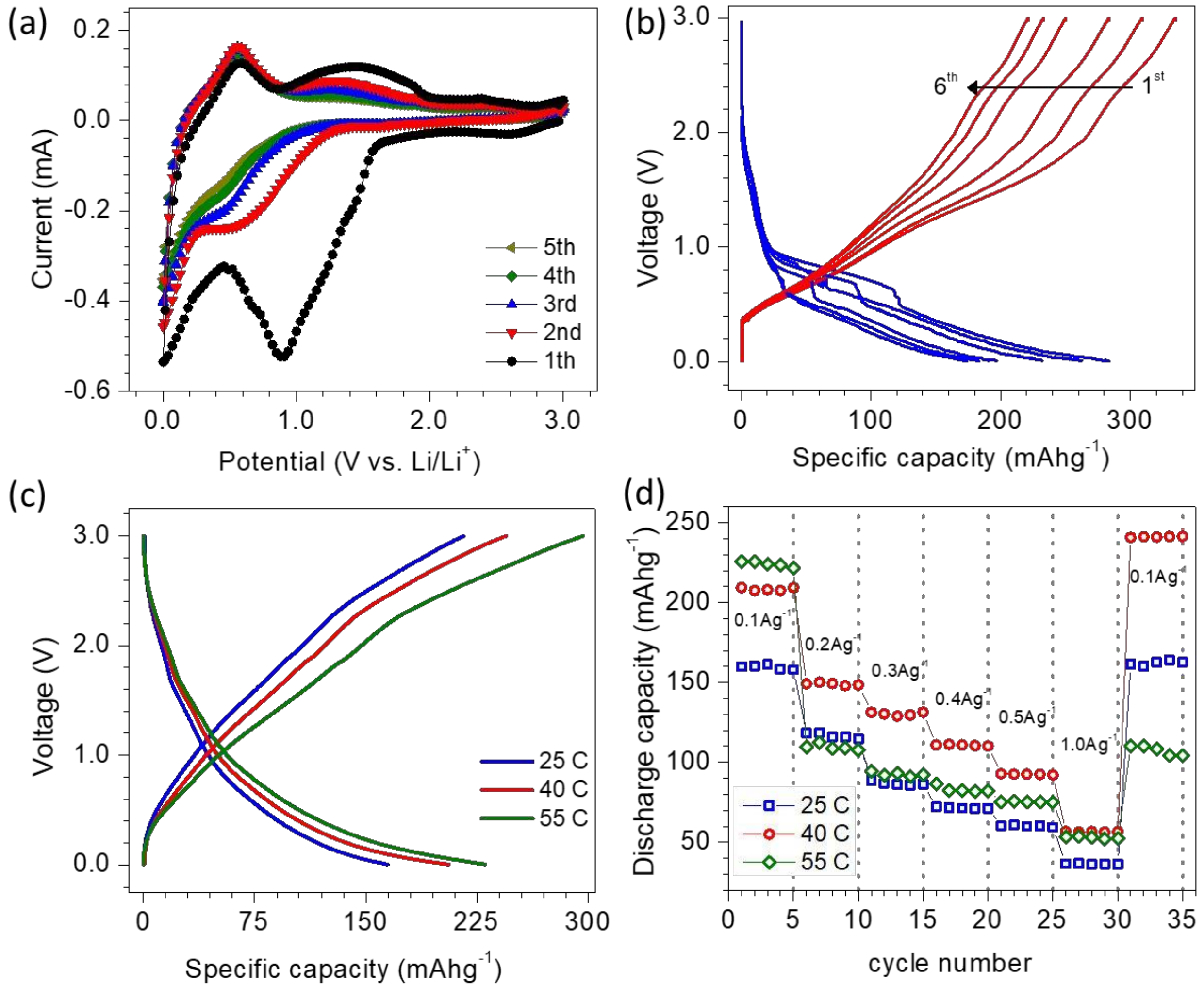

Figure 4. (a) First five cyclic-voltammetry (CV) curves of the CFTS at 25 C and a scan rate of 0.1 mVs ^{1}. (b) Galvanostatic charge ïdischarge (GCD) characteristics of the CFTS at a current of 0.1 Ag ^{1} over the first five cycles. Effect of operating temperature (25, 40, and 55 C) on (c) GCD measurements and (d) rate performances at different currents.

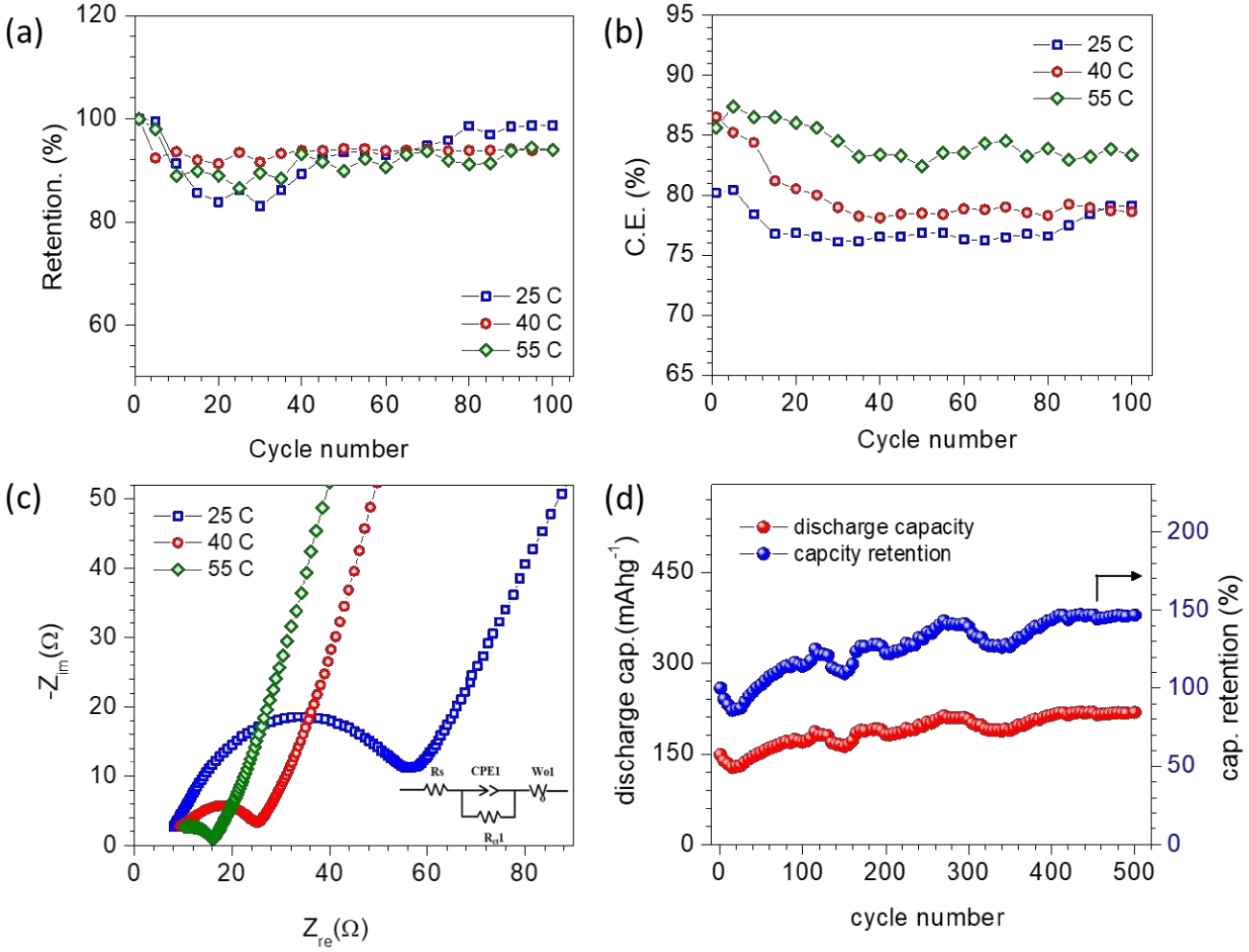

Figure 5. Long-life-cycling performance of the CFTS anode at different operating temperatures: (a) discharge capacity retention (b) Coulombic efficiency. (c) Nyquist plots at different operating temperatures, revealing changes in the charge transfer resistances and reaction kinetics of the CFTS. The inset shows the equivalent-circuit diagram. (d) The room temperature testing of the CFTS for 500 cycles at a current 0.1 Ag ^{1}.

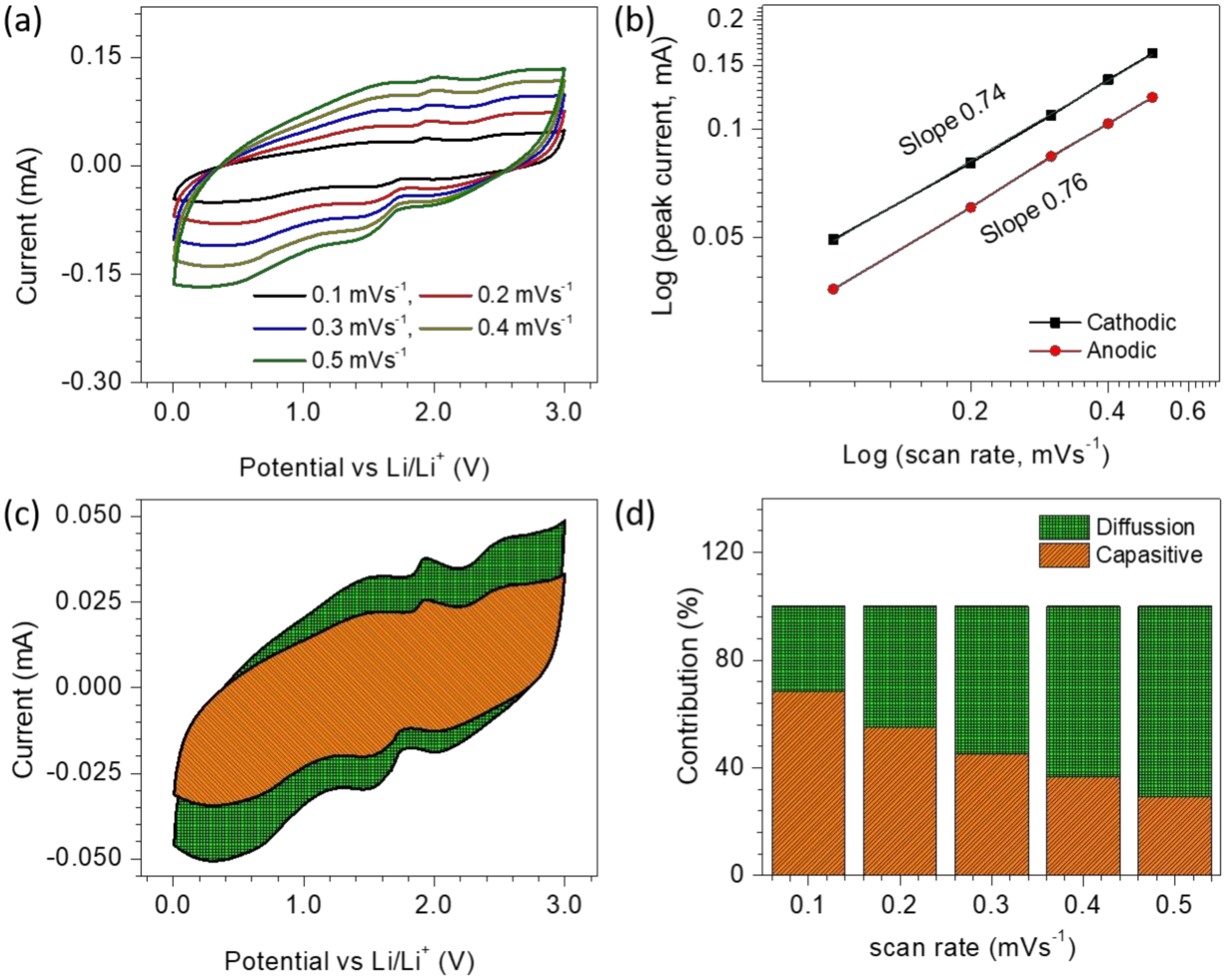

Figure 6. (a) Cyclic-voltammetry (CV) curves at scan rates of 0.1, 0.2, 0.3, 0.4, and 0.5 mVs ^{1}. (b) Plot of log (*i*) vs log ( ), which clarifies the charge storage mechanism of the electrode. (c) CV curves show the capacitive and diffusion-controlled currents recorded at a scan rate of 0.1 mVs ^{1}. (d) The contributions of the storage mechanism at different scan rates.